Dual MOF-derived Fe/N/P-tridoped carbon nanotube as high-performance oxygen reduction catalysts for zinc-air batteries

Hui Chang [a], Ya-Fei Guo [a,c], Xu Liu [a,c], Peng-Fei Wang [c], Ying Xie [b,c,*], Ting-Feng Yi [a,c,**]

[a] School of Materials Science and Engineering, Northeastern University, Shenyang 110819, PR China
[b] Key Laboratory of Functional Inorganic Material Chemistry, Ministry of Education, School of Chemistry and Materials Science, Heilongjiang University, Harbin 150080, PR China
[c] Key Laboratory of Dielectric and Electrolyte Functional Material Hebei Province, School of Resources and Materials, Northeastern University at Qinhuangdao, Qinhuangdao 066004, PR China

ARTICLE INFO

ABSTRACT

The controllable construction of Fe,N co-doped carbon (Fe-N-C) nanocomposite has highly potential in replacing the noble metal catalysts. Herein, the Fe/N/P-tridoped expanded carbon nanotubes (P-Fe-N-CNTs) are prepared according to a simple one-step pyrolysis procedure. The unexpanded Fe-N-C carbon nanotubes (Fe_u-N-CNTs) are also fabricated for comparision. The expanded P-Fe-N-CNTs yields a high half-wave potential ($E_{1/2}$) of 0.8843 V compared with unexpanded Fe_u-N-CNT and commercial Pt/C. Furthermore, the expanded P-Fe-N-CNT as catalyst of Zn-air battery achieves high electrocatalytic performance, which is better than commercial Pt/C material. The unique architecture of expanded P-Fe-N-CNTs can improve the specific surface area and promote the formation the abundant active site, thus promoting the ORR kinetic process. Density functional theory (DFT) calculations futher confirm that suitable P doping can regulate the electronic structures of the active catalytic sites. The work provides a controllable way to prepare rational expanded P-Fe-N-CNTs for different applications, especially in Zn-air battery.

1. Introduction

Global concern of excessive energy consumption and fossil fuels exhaustion cause the booming development of renewable next-generation energy conversion and storage technology. Zinc-air battery (ZAB) is considered as a new promising energy storage device for electric vehicles due to its environmental friendliness, low cost, abundant resources and high theoretical energy density [1,2]. However, the performance of ZAB highly relies on the cathodic samples to overcome the slow oxygen reduction reaction (ORR) [3]. Pt-based catalysts are effective oxygen reduction catalysts. However, the device is far from affordable for wide-scale implementation owing to their expensive price, scarcity and low durability. Therefore, it has become a trend to explore Pt-free ORR electrocatalysts with cost controlled, high-activity and approving stability. Among many non-noble metal ORR catalysts, Fe-N-C has been extensively investigated because of its advantages, such as low price and excellent ORR performance [4,5]. Fe-N-C samples are

usually obtained according to the heat treatment of precursors containing N, C and Fe salts at high temperatures [6,7]. However, the preparation method often leads to unevenly morphology, which hinders charge transfer channels and reduces the utilization efficiency of catalytic centers.

The ideal Fe-N-C ORR electrocatalyst can be obtained according to accurate control of composition and morphology [8,9]. The active sites can be used to evaluate the performance of catalysts, and the catalysts with more and uniform active sites accompanied by an appearance of few metal or carbide nanocrystal particles often possesses a good composition [10]. The effect of particle size on catalyst performance has been in-depth investigated, but the research is limited and needs to be further revealed. Due to the one-dimensional (1D) morphology, carbon nanotubes have some advantages, such as large specific surface area (SSA) and good electronic conductivity [11]. Especially, the carbon nanotubes with uniform morphology, large SSA and abundant porous structure can decrease the charge transfer resistance and increase the

---

* Corresponding author at: Key Laboratory of Functional Inorganic Material Chemistry, Ministry of Education, School of Chemistry and Materials Science, Heilongjiang University, Harbin 150080, PR China.
** Corresponding author at: School of Materials Science and Engineering, Northeastern University, Shenyang 110819, PR China.
E-mail addresses: xieying@hlju.edu.cn (Y. Xie), tfyihit@163.com (T.-F. Yi).

stability of ORR reaction [12]. The composition and morphology regulation are significant factors to achieve excellent ORR electrocatalytic activity [13]. However, the systematic tuning of Fe-N-C samples with both good morphology and composition is a great challenge because these requirements are difficult to be met simultaneously [14]. Therefore, the selection and binding of Fe-, C- and N- precursors during active site formation are of great significance.

Metal-organic frameworks (MOFs) are remarkable precursors for the preparation of efficient M-N-C (M=Fe, Co, Mn, etc) catalysts for ORR process [15]. The reason is that MOFs not only bind to metal nodes bridged by organic ligands to provide transition metals (TM), carbon, and heteroatoms required for catalysis, but also have a controlled periodicity [16,17]. During the carbonization process, the organic ligand converts to porous graphite carbon matrix and the metal ions transforms to metal nanoparticles (MNPs), metal compound nanoparticles (MCNPs) or metal atoms, whcih are embedded in carbon materials (MACs) [18–21]. ZIF-8 usually acts as a N-C precursor. In particular, the Zn evaporates at around 900 ℃ to form many pores, which increases the SSA of material and thus improves the diffusion of gas [22]. As a special type of MOFs, Fe-based Materials of institute Lavoisier framework (MIL) has rich and uniformly dispersed iron atoms [23]. However, the morphology and porous structure of MIL may collapse at the high temperature carbonization stage, resulting in the decrease of the SSA of MIL derived carbon and the aggregation of Fe nanoparticles [24]. Moreover, the preparation of Fe-N-C material used MIL-101 as raw material usually requires the introduction of additional N sources due to the lack of N element in most MIL-101 [25]. Recent studies show that the combination of different types of MOFs materials can take full advantage to promote the controllable formation of oxygen reduction catalysts with different morphologies [16,20]. The method of preparing carbon nanotubes by combining ZIF-8 with different iron sources has been reported [26,27]. However, the synthesis process is too complicated, which requires secondary high temperature pyrolysis and acid treatment. Thus, the preparation method is not conducive to large-scale production [28]. It has been proposed that heteroatom doping can regulate the electronic structure around the active center of Fe atoms and futher enhance the ORR performance. At present, the influence of the addition of heteroatoms on the central metal atoms has been deeply studied, but the the effect of addition amount of heteroatoms on the ORR performance of catalyst is rarely reported. Hence, developing precise amount heteroatom doped Fe-N-C nanotubes with simple synthesis process for high-efficiency oxygen reduction process is very necessary.

In conclusion, we prepared a Fe/N/P-tridoped expanded carbon nanotube (P-Fe-N-CNTs) electrocatalyst with large SSA and abundant porous structure according to a facile one-step calcination way. The NaH$_2$PO$_2$ was served as P source and reductant to promote the formation of expanded P-Fe-N-CNTs catalyst. The high-performance electrocatalysts can be obtained through only one calcination process, without additional acid treatment and secondary calcination process. The resulting expanded P-Fe-N-CNTs are obtained due to the introduction of NaH$_2$PO$_2$, which accelerate the conversion of Fe species in MIL-101 (Fe), thus catalyzing the in-situ growth of carbon nanotubes. At the same time, partially P atoms are embedded into expanded carbon nanotube and provide abundant anchoring sites to capture metal Fe, thus increasing the number of active sites. The DFT results also confirm that proper P-doping into carbon nanotubes can modulate the electronic structures of active centers and therefore enhance the ORR performance. For comparision, common Fe$_u$-N-CNTs samples are also prepared according to a one-step calcination. The expanded P-Fe-N-CNTs sample displays better ORR and ZABs performance than common Fe$_u$-N-CNTs and commercial Pt/C, which can be attributed to the unique expanded nano-bamboo carbon nanotube structure and P doping partially.

2. Experimental section

2.1. Preparation of MOF precursors

The Zn(NO$_3$)$_2$·6 H$_2$O (2.5 g) was added to 75 ml methanol and stirred for 10 min to form solution A. Solution B was formed by stirring 5.519 g 2-methylimidazole in 75 ml methanol solution. Solution B was then poured into solution A and reacted for 4 h at room temperature. The white product was centrifuged and cleaned three times with methanol. The final product ZIF-8 was obtained by vacuum drying at 60 ℃ for 12 h.

The FeCl$_3$·6 H$_2$O (0.675 g) and terephthalic acid (0.2075 g) were added into 15 ml N,N-dimethyl formamide (DMF) solution to obtain a uniform yellow solution. Then the yellow solution was reacted at 110 ℃ for 20 h by a solvothermal reaction. The product was collected and cleaned by DMF and 60 ℃ anhydrous ethanol for several times. The obtained MIL-101(Fe) powder was collected by drying in a vacuum oven at 60 °C for 24 h.

2.2. Preparation of Fe$_u$-N-CNTs and expanded P-Fe-N-CNTs

The Fe$_u$-N-CNTs materials were obtained according to a common calcination process. ZIF-8/MIL-101(Fe) with different mass ratios (300/0, 300/5, 300/15, 300/25 and 300/40) were mechanically mixed with mortar for 0.5 h. The mixture was placed in a quartz tube furnace at 900 ℃ in Ar atmosphere for 3 h. The obtained products were labeled N$_{900}$-C, Fe-N-C-5, Fe-N-C-15, Fe$_u$-N-CNTs and Fe-N-C-40, respectively.

Expanded P-Fe-N-CNTs was synthesized according to the similar way as the preparation of Fe$_u$-N-CNTs catalyst. ZIF-8/MIL-101(Fe) at a mass ratio of 300:25 was mechanically mixed for 0.5 h and then transferred to the downstream of the quartz boat. Sodium monophosphate (NaH$_2$PO$_2$) at a mass of 10 mg was placed upstream of the quartz boat and calcined for 3 h at 900 °C under Ar atmosphere. The resulting sample was named P-Fe-N-CNTs. The different mass of NaH$_2$PO$_2$ was labeled P-Fe-N-C-2 (2 mg) and P-Fe-N-C-20 (20 mg).

2.3. Electrochemical measurements

Electrochemical oxygen reduction reactions (ORR) were tested in a rotating ring-disk electrode (RRDE-3A ALS) and a Ivium VC electrochemical station. The as-synthesized sample, Hg/HgO electrode and Pt wire were used as the working electrode, reference electrode and counter electrode, respectively. The KOH solution of 0.1 M (pH=13) was used as the electrolyte for all ORR measurements. The catalyst ink was obtained by ultrasonic dispersion of sample (2.5 mg) in 20 μl Nafion solution (5 wt%), 300 μl water and 180 μl isopropyl alcohol. The 20% Pt/C was the benchmarking catalyst.

The number of electron transfers (*n*) were obtained from the Koutecky-Levich (K-L) plots by the following equations:

$$\frac{1}{j} = \frac{1}{j_k} + \frac{1}{j_L} = \frac{1}{B\omega^{1/2}} + \frac{1}{j_k} \tag{1}$$

$$B = 0.2nFC_0D_0^{2/3}v^{-1/6} \tag{2}$$

The *n* and H$_2$O$_2$ yield (H$_2$O$_2$%) were calculated according to RRDE tests by the following equations:

$$H_2O_2(\%) = 200 \times \frac{\frac{I_r}{N}}{I_d + \frac{I_r}{N}} \tag{3}$$

$$n = 4 \times \frac{I_d}{I_d + \frac{I_r}{N}} \tag{4}$$

Details of the above experimental tests and explanations of the equations were given in the supporting information.

2.4. Zn-air battery (ZAB) measurements

ZAB were mainly composed of a Ni foam containing a catalyst (cathode) and a polished Zn sheet (anode, length×width×thickness = 85 ×34 ×0.5 mm^3). The electrolyte was a mixture of 6 M KOH and 0.2 M Zn (Ac)$_2$. The catalyst load was 1 mg cm^{-2}. The polarization curve of ZAB was evaluated by linear sweep voltammetry (LSV) testing at 10 mV s^{-1}. The galvanostatic discharge measurements were tested at 10 mA cm^{-2}. Electrochemical impedance spectrum (EIS) was obtained in the frequency range from 10^5 to 0.01 Hz.
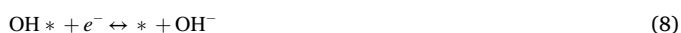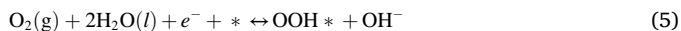
2.5. Computational models and methods

All density functional theory (DFT) calculations were performed by using the Vienna ab initio simulation package (VASP) [29–32]. With the application of the projector augmented-wave (PAW) technique [33], Perdew-Burke-Ernzerhof (PBE) functional [34] were applied. The plane-wave energy cutoff was 500 eV, and the (3 ×3 ×1) Monkhorst-Pack mesh [35] was used to deal with the sampling over Brillouin zone. The convergence criterions during calculations were 10^{-5} eV for the energies and − 0.01 eV/Å for the forces. To avoid the fake interactions along c axis, a vacuum slab with a thickness of 15 Å was considered.

To evaluate the structure stability, relevant models were constructed and the formation energy was then calculated according to the total energies of the (P-doped) Fe-N-C systems with respect to those of elemental phase such as N$_2$ gas molecule, C atom in graphite, and P elementary substance. The model details are presented in the supporting information. For ORR in alkaline condition, the overall reaction can be expressed as follow,

$$O_2 + 2H_2O + 4e^- \leftrightarrow 4OH^-$$
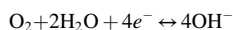
The above reaction is composed of four elementary steps,

$$O_2(g) + 2H_2O(l) + e^- + * \leftrightarrow OOH* + OH^- \tag{5}$$

$$OOH* + e^- \leftrightarrow O* + OH^- \tag{6}$$

$$O* + H_2O(l) + e^- \leftrightarrow OH* + OH^- \tag{7}$$

$$OH* + e^- \leftrightarrow * + OH^- \tag{8}$$

where * represents the active site on the catalyst surface, (l) and (g) denotes liquid and gas phases, respectively. According to the reversible hydrogen electrode (RHE) model [36], the Gibbs reaction free energy of each elementary step under different PH and output potential can be calculated. For the free energy of different adsorption systems, the zero-point energy of the intermediates are calculated, while the entropy contributions of different free molecules are taken from the experimental data. Furthermore, as the exact free energies of OOH, OH, and O radicals are difficult to obtained, the adsorption free energies of ΔG_{OOH*}, ΔG_{O*} and ΔG_{OH*}, which were calculated according to the energy references of H$_2$O(g) and H$_2$(g), were introduced [37]. Under this circumstance, the reaction free energy of Eq.(9) - Eq.(12) can be calculated by,

$$\Delta G_1 = \Delta G_{OOH*} - 4.92 \tag{9}$$

$$\Delta G_2 = \Delta G_{O*} - \Delta G_{OOH*} \tag{10}$$

$$\Delta G_3 = \Delta G_{OH*} - \Delta G_{O*} \tag{11}$$

$$\Delta G_4 = -\Delta G_{OH*} \tag{12}$$

The onset potential can be calculated by,

$$U_{RHE}^{onset} = - \max\{\Delta G_1, \Delta G_2, \Delta G_3, \Delta G_4\} \tag{13}$$

The over potential (η) is calculated by,

$$\eta = 1.23 - U_{RHE}^{onset} \tag{14}$$

## 3. Results and discussion

3.1. Structure and composition analysis

The preparation diagram of P-Fe-N-CNTs catalysts are simply illustrated in Scheme 1. The highlight of this work is to achieve the regulation of carbon nanotubes with high catalytic activity by one-step calcination without additional acid treatment. Firstly, MIL-101 (Fe) is chosen as the Fe source instead of the traditional inorganic Fe source. The reason is that MIL-101(Fe) has a high SSA, evenly dispersed Fe^{3+} and abundant porous structure, which provides a good channel for electron transfer in ORR process. Additional adding NaH$_2$PO$_2$ during calcination is a vital procedure to synthesize expanded carbon nanotubes. NaH$_2$PO$_2$ decomposes at high temperature to produce PH$_3$ gas, which can introduce P atoms into the carbon structure and capture the Fe elements to form Fe$_2$P nanoparticles [38]. And the transient release of PH$_3$ at high internal pressure is conducive to the formation of defect-rich carbon structure.

The XRD pattern confirms the successful synthesis of ZIF-8 and MIL-100 (Fe), which is highly consistent with the standard MOF pattern [13] (Fig. S1). The XRD patterns of the as-obtained N$_{900}$-C, Fe$_u$-N-CNTs and P-Fe-N-CNTs samples are displayed in Fig. 1a. Two diffraction peaks at about 26° and 44° can be found in N$_{900}$-C, which can be attribute to the amorphous C structure [39]. The peak of Fe$_u$-N-CNTs at about 26.2° represents the (002) planes of graphite carbon. The graphitization degree of carbon gets stronger as the precursor MIL-101(Fe) increases (Fig. S2). Moreover, two peaks at 44.6° and 43.7° in Fe-N-C-40 sample can be obviously observed corresponding to metallic Fe (PDF#06–0696) and Fe$_3$C (PDF#35–0772), respectively [4,40]. This result indicates that high Fe content improves the graphitization degree of carbon, resulting in potentially high electronic conductivity and excellent corrosion resistance of the sample. Small amounts of Fe$_3$C were also found in P-Fe-N-CNTs as described previously (Fig. 1a and Fig. S3a). The peak intensity of Fe$_3$C increases in P-Fe-N-C-20 sample as the increase of NaH$_2$PO$_2$ (Fig. S3b), indicating that the excessive NaH$_2$PO$_2$ promotes the formation of Fe$_3$C nanoparticles. However, the P related species are not found in XRD pattern of P-Fe-N-CNTs samples because the small amount of P loading may not meet the minimum detection for XRD.

The structural defects and graphitization degree of the N$_{900}$-C, Fe$_u$-N-CNTs and P-Fe-N-CNTs are investigated by Raman spectroscopy. Two distinct peaks at 1350 cm^{-1} (disordered carbon, D band) and 1580 cm^{-1} (graphitic carbon, G band) can be found in Fig. 1b [41]. The defect and graphitization degree of carbon sample can be characterized by the relative intensity ratio of D band and G band (I_D/I_G). Compared with N$_{900}$-C (1.07), Fe$_u$-N-CNTs (0.76) and P-Fe-N-CNTs (0.92) have a lower I_D/I_G value, indicating that the Fe doping from MIL-101(Fe) enhances the graphitization degree of the samples. The result is consistent with XRD analysis. After adding NaH$_2$PO$_2$, the I_D/I_G value of Fe$_u$-N-CNTs increases by 0.16, indicating that the number of defects in P-Fe-N-CNTs increases. This is due to the successful introduction of P elements into the Fe$_u$-N-CNTs sample, resulting in the deformation of the sp^2 carbon lattice inside the sample. Therefore, the introduction of appropriate NaH$_2$PO$_2$ during calcination process can increase the number of defects in the material. More defects can promote the effective utilization of active center, which is conducive to improving the ORR.

The N$_2$ adsorption-desorption isotherms (NADI) of the catalysts are observed in Fig. S4a, which can be used to evaluate the SSA and porous structure distribution of the material. The NADI of all the materials exhibit similar type-IV curves, depicting a hysteresis loop at high N$_2$ partial pressure and a sharp rise at low relative pressure [42]. The results indicate that the samples simultaneously exist inherent micropore and mesopore characteristics. The micropores are mainly from the evaporation of Zn. The Brunauer-Emmett-Teller (BET) SSA of samples is
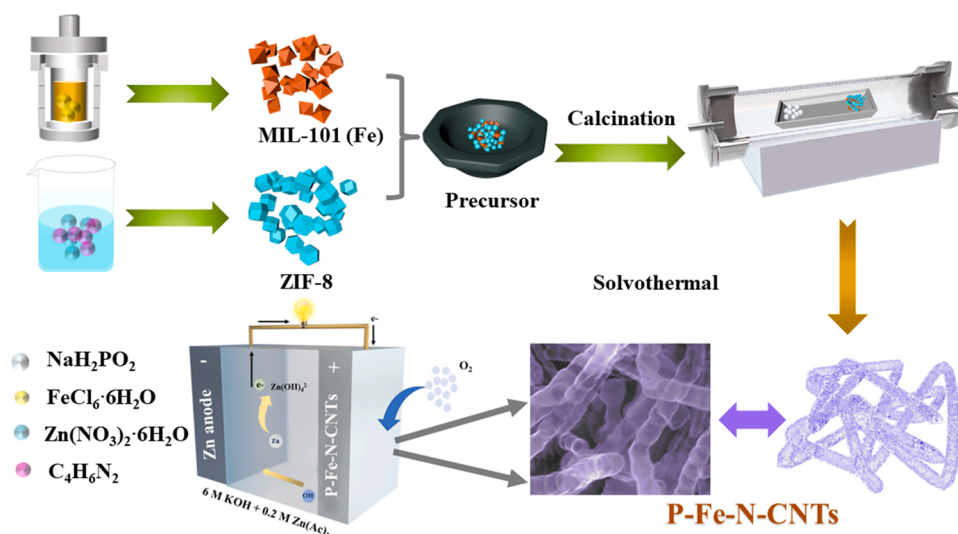
Scheme 1. Schematic diagram of the synthesized procedure of expanded P-Fe-N-CNTs.

summarized in Table S1. The SSA of N_{900}-C, Fe_u-N-CNTs and P-Fe-N-CNTs are 537.3, 575.2 and 599.8 $m^2\,g^{-1}$, respectively. It can be inferred that the formation of carbon nanotubes increases the SSA of Fe_u-N-CNTs and P-Fe-N-CNTs. Compared with the Fe_u-N-CNTs, the SSA of P-Fe-N-CNTs increases significantly, which may be caused by the expansion of CNTs structure. The size distribution of the sample can be estimated according to H-K method (micropores) and BJH method (mesopores) (Fig. S4b,c). The rich micropores in P-Fe-N-CNTs provide sufficient hosts for catalytic centers. The existence of mesoporous structure can reduce the mass transport resistance and enhance the catalytic performance [27]. Therefore, the large SSA, appropriate pore volume and pore structure in P-Fe-N-CNTs sample can provide an excellent mass transfer channel to accelerate the electron transfer process, thus improving the ORR process.

XPS is used to evaluated the element composition and chemical valence states of catalysts. The XPS survey spectra of N_{900}-C, Fe_u-N-CNTs and P-Fe-N-CNTs are shown in Fig. S5. N_{900}-C, Fe_u-N-CNTs and P-Fe-N-CNTs also have similar peaks of Zn, C, N, and O, except for the additional Fe 2p peaks in Fe_u-N-CNTs and P-Fe-N-CNTs. The existence of P is not observed in the XPS spectrum (Fig. S5), which may be due to the fact that P is encapsulated inside the carbon nanotubes. Because XPS is a surface analysis method, it is difficult to detect the P element encapsulated in carbon nanotubes through XPS test. However, ICP test shows that the mass fraction of P in the P-Fe-N-CNTs is 0.055%, which confirms the existence of P. Atomic percentage of the above three catalysts are shown in Table S2. The contents of Fe (1.62 at%) and N (8.85 at%) in P-Fe-N-CNTs are obviously increase compared with Fe_u-N-CNTs electrocatalyst (Fe: 1.34 at%, N: 7.31 at%) due to the introduction of NaH_2PO_2. The results demonstrate that the introduction of NaH_2PO_2 changes the electronic environment and content of N and Fe, which is beneficial to obtain excellent catalytic performance.

The peaks of Fe 2p deconvolution spectrum in Fe_u-N-CNTs and P-Fe-N-CNTs samples include $2p_{3/2}$ (710.7 eV) and $2p_{1/2}$ (724.2 eV) of Fe-N_x (Fig. 1c) [15–17]. An additional peak center for P-Fe-N-CNTs sample at 704.7 eV is ascribed to Fe-P bond, further confirming the existence of the Fe_2P species [38,43]. Fig. 1d also shows the deconvolution spectra of N 1 s for N_{900}-C, Fe_u-N-CNTs, and P-Fe-N-CNTs. The N 1 s peaks of N_{900}-C contain pyridinic-N (398.6 eV), pyrrolic-N (400.1 eV), graphitic-N (401.1 eV) and oxidized-N (403.2 eV) [17]. The N 1 s spectra of Fe_u-N-CNTs and P-Fe-N-CNTs show an additional fitting peak at 399.2 eV, corresponding to Fe-N_x. Previous studies have shown that the binding energies of pyridinic-N and metal-N are very similar in numerous N-doped samples. This is due to the fact that Fe-N_x can provide partial pyridinic-N, and the two can be transformed into each other.

The high content of pyridine-N and metal-N can enhance electron transport in ORR process according to lowering the energy barrier for adjacent carbon atoms to absorb O_2. Graphitic-N can increase the electronic conductivity and electron transfer ability of the sample. The N 1 s surface atomic percentage of the above three samples is shown in Table S3. Interestingly, the graphite N content increases from 19.1% of Fe_u-N-CNTs to 22% of P-Fe-N-CNTs, the pyridine N content increases from 30.3% of Fe_u-N-CNTs to 30.6% of P-Fe-N-CNTs, and the Fe-N_x content increases from 19.1% of Fe_u-N-CNTs to 22% of P-Fe-N-CNTs. Fig. 1e shows the C 1 s XPS spectrum of N_{900}-C, Fe_u-N-CNTs and P-Fe-N-CNTs. For P-Fe-N-CNTs, it has five fitting peaks of 283.9 eV (C-P), 284.7 eV (sp^2-C), 285.6 eV (sp^3-C), 286.8 eV (C-N_x) and 288.4 eV (C-O/C=O), demonstrating that P and N elements have been doped into carbon nanotube [38]. The ORR performance can be improved according to the existence of C-P bond. The sp^2-C represents graphite C, and the atomic percentage of sp^2-C in P-Fe-N-CNTs, Fe_u-N-CNTs and N_{900}-C is 50.7%, 58.6% and 48.1% (Table S4), respectively, indicating that the addition of Fe induces a higher graphitization level. The result is consistent with the Raman spectra. The C-N_x bond can also be used as catalytic center of ORR. The atomic percentage of C-N_x in P-Fe-N-CNTs, Fe_u-N-CNTs and N_{900}-C is 21%, 8.7% and 7%, respectively. Therefore, the P-Fe-N-CNTs exhibits the abundant C-N_x, suitable graphite C, additional C-P sites and Fe_2P species. The results further confirm that P-Fe-N-CNTs sample has excellent ORR dynamics.

The spin state of Fe specie in P-Fe-N-CNTs can be characterized by ^{57}Fe Mössbauer spectroscopy. Fig. 1f and Table S5 show that the ^{57}Fe Mössbauer spectra of P-Fe-N-CNTs can well fit one singlet (singlet 1), four doublets (D1, D2, D3 and D4) and one sextet (sext 1) [16,20,44]. The three doublets denoted as D1, D2 and D3 belong to the low spin Fe (II)-N_4, medium spin Fe (II)-N_4 and high spin N-Fe (II)-N_4/C, respectively. A sextet (Sext 1) corresponding to Fe_3C is also detected [45]. One singlet (singlet 1) and doublets (D4) can be assigned to Fe_2P, which account for only 11.44% of the total Fe species. Therefore, the Fe_2P cannot be detected by XRD. Namely, the Fe element in P-Fe-N-CNTs is mainly composed of three states: Fe_3C, Fe_2P and Fe (II)-N_4.

3.2. Morphology analysis

Fig. S6a exhibits the SEM image of ZIF-8, which has a classic rhombohedral crystal structure with an average size of 100–200 nm. MIL-101 (Fe) exhibits a common zeolite octahedral structure with diameters ranging from 400 to 600 nm (Fig. S6b). Interestingly, Fe-N-C-5 maintains the rhombohedral morphology of ZIF-8 with a homogeneous distribution after pyrolysis (Fig. S7a). However, with the content of MIL-
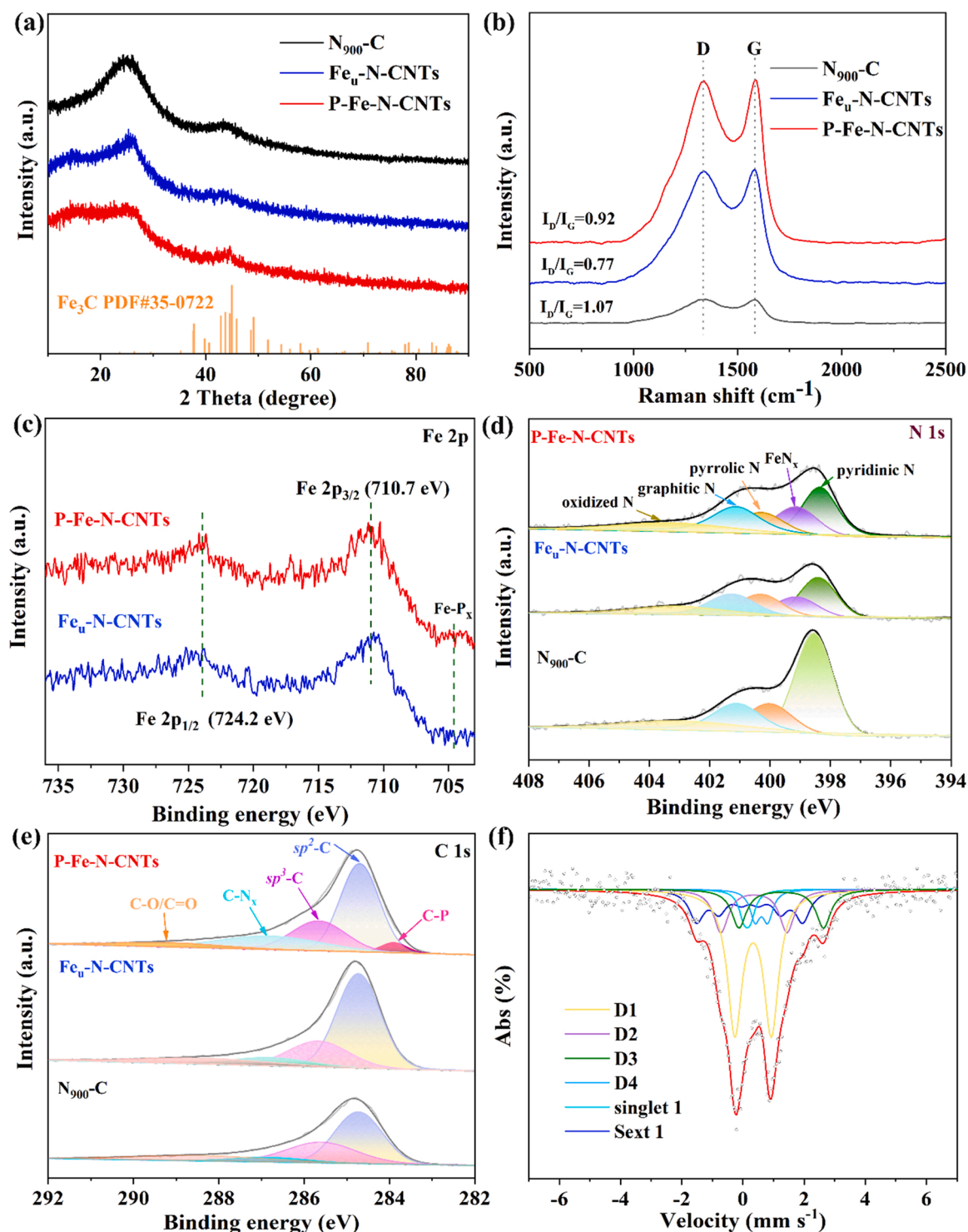
Fig. 1. (a) XRD patterns and (b) Raman spectra and (c-e) high-resolution XPS spectrum of N_{900}-C, Fe_u-N-CNTs and P-Fe-N-CNTs; (f) ^{57}Fe Mössbauer transmission spectrum of P-Fe-N-CNTs measured at 293 K.

101(Fe) increases, Fe-N-C-15 samples begin to distort (Fig. S7b). When the ratio of MIL-101(Fe) to ZIF-8 increases from 25:300–40:300, the morphology of the sample is restructured to form carbon nanotubes with different sizes (Fig. 2a and Fig. S7c). Fe_u-N-CNTs catalyst shows a morphology of carbon nanotubes with an average thickness of 25–35 nm in Fig. 2a. The successful synthesis of Fe_u-N-CNTs is also demonstrated according to TEM image (Fig. 2c). The results show that appropriate Fe content is very important for the formation of carbon nanotubes. TEM images show that several small particles are incorporated inside the sample. From the HRTEM images performed on individual particles of Fe_u-N-CNTs (Fig. 2d,e), it can be found that the spacing of 0.2026 nm corresponds to the (110) lattice fringe of metallic Fe, and the spacing of 0.2013 nm corresponds to the (031) lattice fringe of Fe_3C [40]. HAADF-TEM is used for elemental analysis of Fe_u-N-CNTs, confirming that the Fe, N and C are uniformly dispersed in carbon nanotubes (Fig. S8). According to previous studies, Fe, Fe_3C and Fe/Fe_3C nanoparticles can become the growth site of carbon nanotubes, which are quickly encapsulated by graphite carbon [46–48]. In our work, we
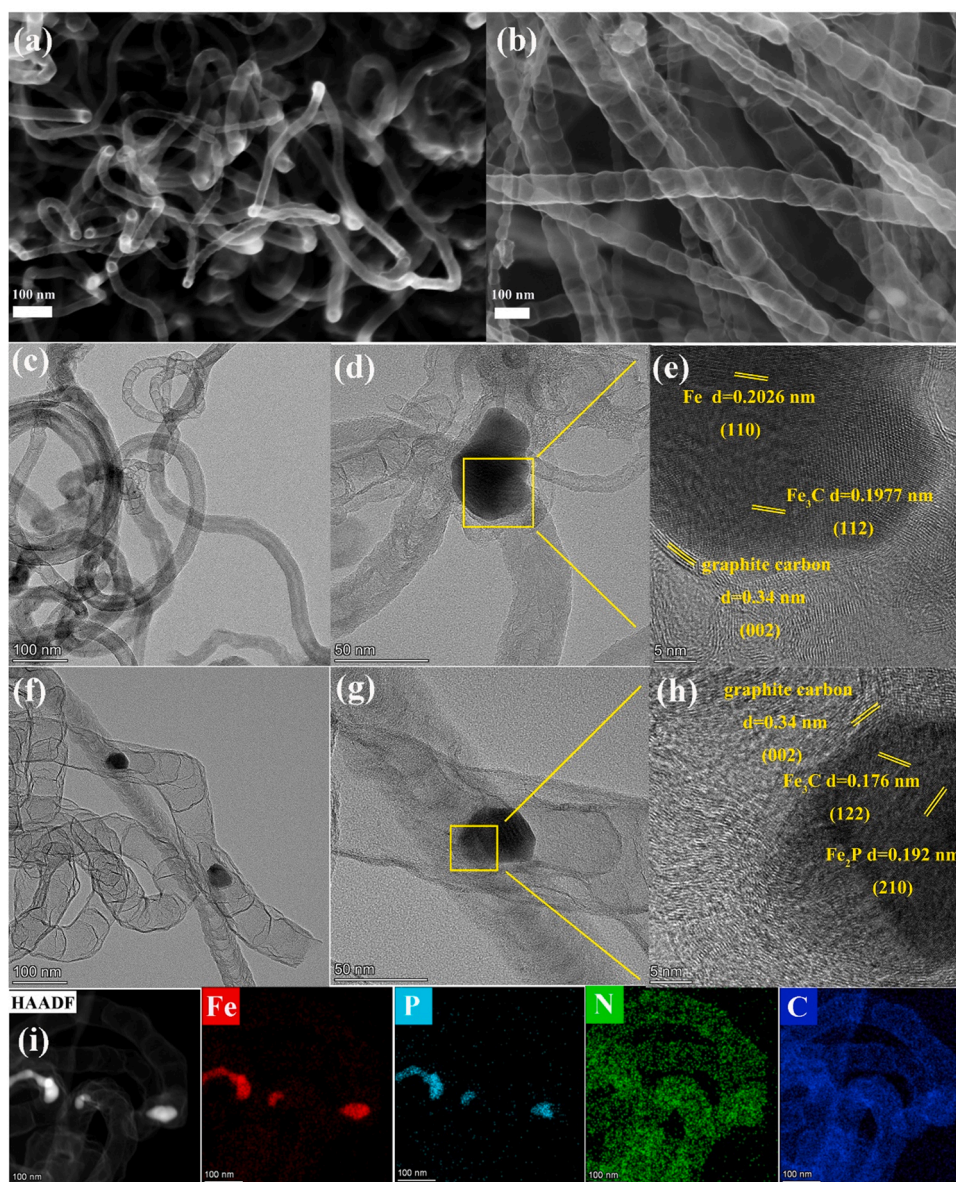
Fig. 2. SEM images of (a) Fe$_u$-N-CNTs, (b) P-Fe-N-CNTs; TEM images of (c-e) Fe$_u$-N-CNTs, (f-h) P-Fe-N-CNTs at different magnifications and (i) TEM elemental mapping images of Fe, P, N and C of P-Fe-N-CNTs.

found that the additional NaH$_2$PO$_2$ promoted the formation of Fe related species and accelerated the growth of carbon nanotubes. Fig. S9a confirms our conclusion that the expansion of nanotube can be found in P-Fe-N-C-2 samples, but excessive NaH$_2$PO$_2$ results in a formation of a large number of Fe$_2$P species, which substitutes the Fe$_3$C growth site of carbon nanotube, thus preventing the formation of carbon nanotubes (Fig. S9b). Fig. 2b,f and Fig. S10 show the successful synthesis of carbon nanotubes with an interesting expanded bamboo morphology. Therefore, NaH$_2$PO$_2$ is innovatively used to regulate the morphology of carbon nanotubes, and the morphology of the synthesized carbon nanotubes is more uniform and controlled. HRTEM images confirm the presence of Fe$_3$C and Fe$_2$P nanoparticles in Fig. 2g,h. HAADF-STEM is used to verify chemical components and element distribution (Fig. 2i). In particular, Fe and P contents in nanoparticles are higher than those in surrounding areas. This strongly demonstrates the presence of Fe$_2$P nanoparticles on the nanotubes. The above results confirm that the morphology of expanded bamboo-carbon nanotube is successfully regulated by the addition of NaH$_2$PO$_2$.

3.3. The role of Fe, N, P and CNTs in electrocatalytic performance

The ratio of ZIF-8 to MIL-101(Fe) and the amount of NaH$_2$PO$_2$ can influence the ORR performance for electrodes. Different ratios of ZIF-8 to MIL-101(Fe) and the amount of NaH$_2$PO$_2$ are discussed by evaluating the ORR activity of samples. The ORR performance is determined by linear sweep voltammetry (LSV). The LSV plots of all catalysts are depicted in Fig. S11 and Fig. S12. Fe$_u$-N-CNTs sample exhibits the highest ORR activity in the series of P-free samples with an onset potential (E_{onset}) of 1.01 V, a $E_{1/2}$ of 0.8733 V and the limited current density (j_L) of -5.75 mA cm^{-2} (Fig. S11). The ORR performance of Fe-N-C-5 and Fe-N-C-15 is degraded. The reason can be ascribed to the low catalytic centers. However, the E_{onset} and $E_{1/2}$ of Fe-N-C-40 catalyst decrease to 0.975 V and 0.8603 V as the Fe content increases, respectively. The reason is that high Fe content results in the agglomeration of Fe species rather than the formation of Fe-N$_x$ active sites. When additional NaH$_2$PO$_2$ is added, the ORR performance of all samples is to some extent superior to Fe$_u$-N-CNTs sample (Fig. S12 and Table S6). And the P-Fe-N-CNTs sample has the best ORR performance among all samples,

which may be due to the generation of expanded carbon nanotubes and the synergistic effect of Fe-N_x/P_x active sites and N-, P-co-doped carbon promotes the ORR performance [49].

Fig. 3a shows the LSV curves of P-Fe-N-CNTs, Fe_u-N-CNTs and Pt/C samples. Expanded P-Fe-N-CNTs sample significantly shows higher E_{onset} (1.04 V), $E_{1/2}$ (0.8843 V) and J_L (−6.4 mA cm^{-2}) than those of Fe_u-N-CNTs sample and commercial Pt/C catalyst. The test results of P-Fe-N-CNTs, Fe_u-N-CNTs and Pt/C are shown in Fig. 3b. This is because the synergistic effect of Fe-N_x/P_x active center and N-, P-co-doped carbon nanotube can quickly activate oxygen molecules [49,50]. Meanwhile, the expanded P-Fe-N-CNTs carbon nanotubes with the highest SSA and most abundant pore structure improve the electron transfer, thus further enhancing ORR performance. The n of each oxygen molecule in ORR is determined by the K-L equation under multiple rotating speeds. And the n values of P-Fe-N-CNTs and Fe_u-N-CNTs are about 3.99 and 3.97, respectively, confirming that the prepared sample is a four-electron transfer path (Fig. 3c,d and Fig. S13). The H_2O_2 yield and n of as-prepared samples can be used to calculate within 0.2 ~ 0.8 V. The H_2O_2% of P-Fe-N-CNTs is significantly better than that of Fe_u-N-CNTs and commercial Pt/C (Fig. 3e), demonstrating that P-Fe-N-CNTs has outstanding selectivity for ORR. In addition, the RRDE measurement results of P-Fe-N-CNTs show that the n value is near to 4.0, further

confirming that P-Fe-N-CNTs follows four-electron path. The Tafel slope of P-Fe-N-CNTs electrode (69 mV dec^{-1}) is smallest (Fig. 3f) among all samples, demonstrating the most excellent ORR dynamic process. P-Fe-N-CNTs not only has outstanding ORR performance, but also has high stability. The stability of P-Fe-N-CNTs and commercial Pt/C was tested by accelerated durability test (Fig. 3g and Fig. S14). The $E_{1/2}$ of P-Fe-N-CNTs shows a negligible loss of 2 mV after 5000 cycles, less than Pt/C of 48 mV, confirming excellent durability performance. The current retention rate of P-Fe-N-CNTs maintains about 96.3% after a continuous test of 10000 s, which is superior than Pt/C (92.1%) (Fig. 3h). The addition of NaH_2PO_2 not only controls the morphology, but also introduces P atoms, which greatly improves the ORR performance of the catalyst. The ORR performance of the electrocatalyst in this work is higher than the results reported in many literatures (Fig. 3i), such as Fe/Fe$_3$C-N-CNTs [10], SAC-FeN-WPC [2], N-rich Fe-N-C [6], Fe, N-CNT/FeNP [12], ZFP-800 [9], Fe$_{NP}$@Fe-N-C [26], ZFN-900 [22], FeCo@NS-CA [43], Fe$_3$C@NC-60–800 [40] and Fe-NCNT [15]. According to the above analysis, the expanded P-Fe-N-CNTs sample possesses excellent activity, high selectivity and strong stability, which shows a promising potential practical application.
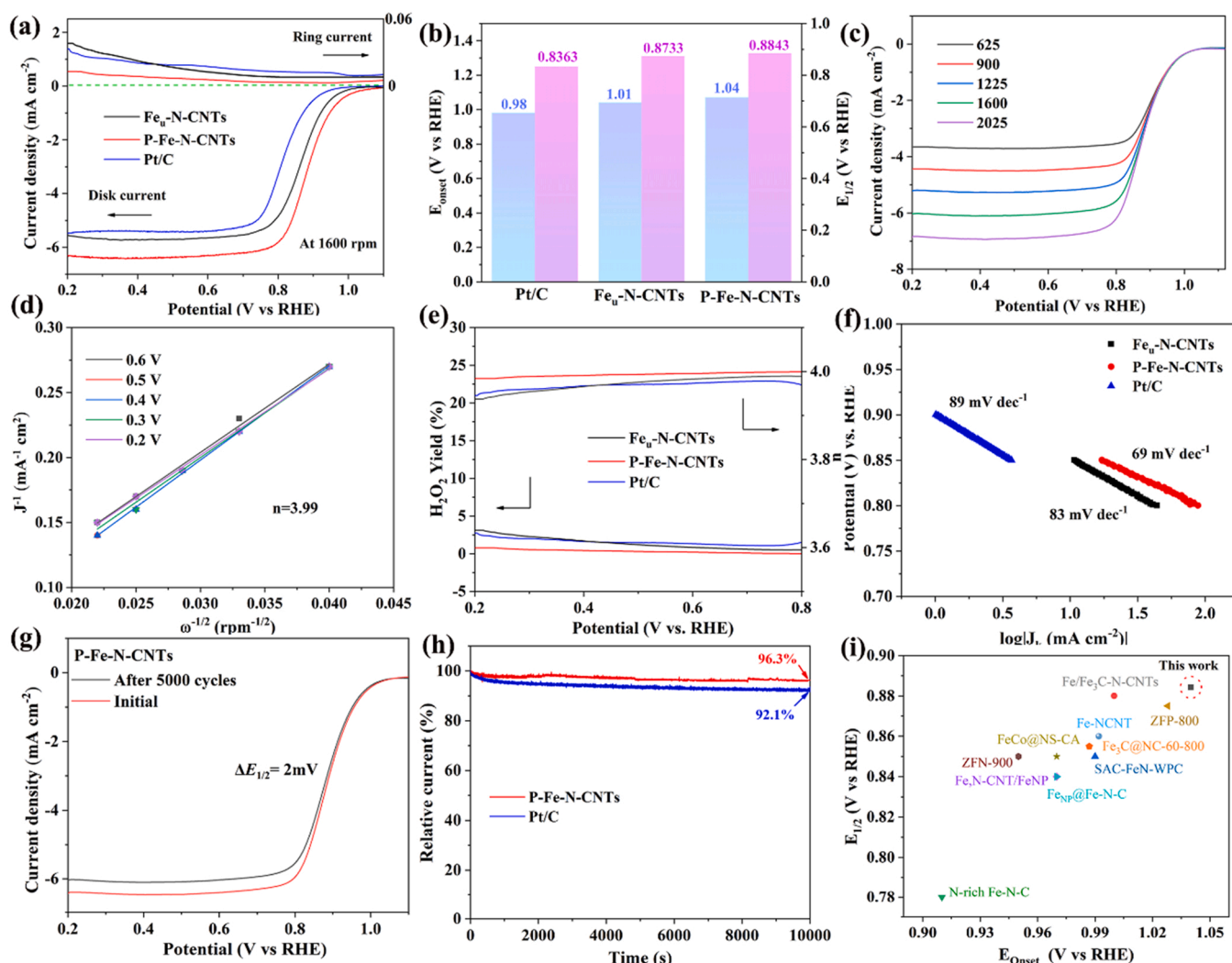

Fig. 3. (a) ORR LSV plots of P-Fe-N-CNTs, Fe_u-N-CNTs and Pt/C and (b) corresponding E_{onset} and $E_{1/2}$; (c) LSV curves of P-Fe-N-CNTs at different rotating speeds, (d) K-L plots of P-Fe-N-CNTs; (e) n and H_2O_2% of P-Fe-N-CNTs, Fe_u-N-CNTs and Pt/C; (f) Tafel plots of P-Fe-N-CNTs; (g) LSV curves before and after 5000 CV cycles of P-Fe-N-CNTs; (h) I-t chronoamperometric response of P-Fe-N-CNTs and Pt/C; (i) comparison of E_{onset} and $E_{1/2}$ of P-Fe-N-CNTs with other advanced electrocatalysts reported in the three years.

3.4. Application of P-Fe-N-CNTs in ZABs

Based on the best ORR performance of P-Fe-N-CNTs in alkaline solution, the practical application potential of P-Fe-N-CNTs is evaluated as an air cathode catalyst in ZABs, and the commercial Pt/C is used as reference object. The detailed assembly process of ZABs can be found in the SI. Fig. 4a shows the structure and key components of ZABs. The P-Fe-N-CNTs air cathode has higher open-circuit voltage (OCV) (1.498 V) than Pt/C (1.47 V) (Fig. 4b). Moreover, the assembled ZABs used P-Fe-N-CNTs air as cathode can light up LED devices with a voltage of 1 V, confirming its potential practical applications (inset of Fig. 4b). From the discharge polarization curve given in Fig. 4c, it can be found that the power density of P-Fe-N-CNTs is 145 mW cm^{-2}, which is significantly better than Pt/C (109 mW cm^{-2}). Meanwhile, the variation of P-Fe-N-CNTs sample is much smaller than Pt/C sample under different current densities, which further proves its excellent rate performance (Fig. 4d). In addition, the durability test is performed at 10 mA cm^{-2} (Fig. 4e). P-Fe-N-CNTs has a satisfactory durability and the voltage retention rate is 95.1% after 144 h. At the same time, the specific capacity of ZABs is evaluated by the consumption of Zn under the condition of constant discharge current density of 10 mA cm^{-2}. The discharge specific capacity of P-Fe-N-CNTs is 885 mAh g^{-1}, which far exceeds than that of Pt/C (824 mAh g^{-1}) (Fig. 4f). The EIS measurement for the catalysts assembled Zn-air battery was shown in Fig. S15. The zinc-air battery used P-Fe-N-CNTs catalyst shows a lower charge transfer resistance than the one used Pt/C catalyst, indicates higher electrochemical reaction activity, which is conducive to the improvement of Zn-air battery performance. The above tests confirm that expanded P-Fe-N-CNTs nanotubes have a potential to replace noble metal catalysts for ZABs.

3.5. Theoretical evaluation on ORR performance

The DFT calculations are used to reveal the underlying ORR mechanism of our P-Fe-N-CNTs catalyst for the first time. Some representative computational models are depicted in Fig. 5, and further details can be displayed in supporting information. Relying on pristine Fe-N-C (FeN$_4$) structure, different amount of P dopants (Fig. 6) is introduced. When P atom substitutes different carbon atoms near nitrogen, the formation energies can be varied from − 6.368 eV to − 6.931 eV (Table S7), and the structure in Fig. 5b is the most stable. The ORR free energy diagrams at U= 0.0 eV and U= 1.23 V are showed in Fig. 5d,e for different catalysts, respectively. The results suggests that when the output potential is zero (U=0.0 V vs. RHE), and the four elementary steps of the ORR process for all considered systems are spontaneous. For pristine Fe-N-C (FeN$_4$) system, when the output potential increases to 0.733 V (Table S8), the free energy of the third elementary step becomes positive, while the values of other elementary steps remain negative, indicating a theoretical E_{onset} of 0.733 V. Fig. 5e further shows that the rate determine step corresponds to the formation of OH* from O* for pristine Fe-N-C catalyst at a output potential of 1.23 V (vs. RHE), as the energy barrier of this step is the largest and calculated to be 0.497 eV (Table S8).

When P dopant is introduced, the adsorption strength of OOH* and OH* intermediates is enhanced (black arrows in Fig. 5d,e), while that of O* one is weakened gradually with increasing P doping amount. Such a result implies that P dopant can modulated the electronic structures of the active catalytic sites and therefore affect the ORR performance of the catalysts. It can be confirmed from Fig. 7a that ΔG_3 increases continuously, while ΔG_4 decreases gradually. Furthermore, the total free energies of the third and fourth elementary steps are close (from −1.562 to −1.635), yet these two steps are inter-inhibitive. As a result, the rate determine step for P-doped Fe-N-C system is thus controlled by the formation of OH- from OH* . At an output potential of 1.23 V (vs. RHE), the over potentials for FeN$_4$-P and FeN$_4$-2 P systems are calculated to be 0.436 and 0.584 eV (Table S8). In comparison to pristine FeN$_4$, the over potential of P-doped systems is reduced by 28 mV first and then enhanced significantly again with increasing P doping amount. Such a variation trend can be illustrated by the electron density differences and Bader charges depicted in Fig. 7b-d and Fig. 8. The introduction of P will lead to a continuous electron transfer from P/Fe to N species, leading to a gradually enhanced or weakened adsorption strength for OH* or O* intermediates, respectively. It should be noted that a large amount of
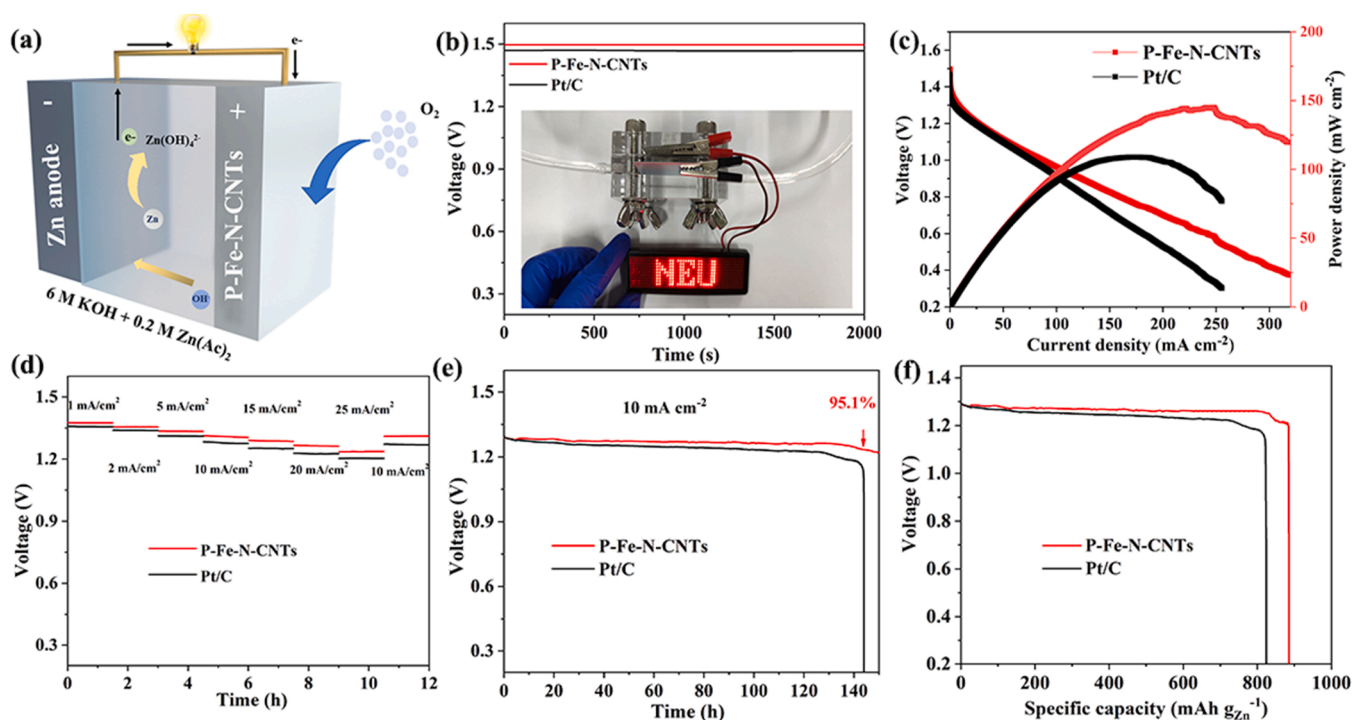

Fig. 4. (a) Schematic diagram of the ZAB. (b) OCV curves and the demonstration of ZAB configuration (inset), (c) Discharge polarization curves, (d) Rate performance, (e) cycle performance at 10 mA cm^{-2} and (f) specific capacity curves at 10 mA cm^{-2} of P-Fe-N-CNTs and Pt/C based ZABs.
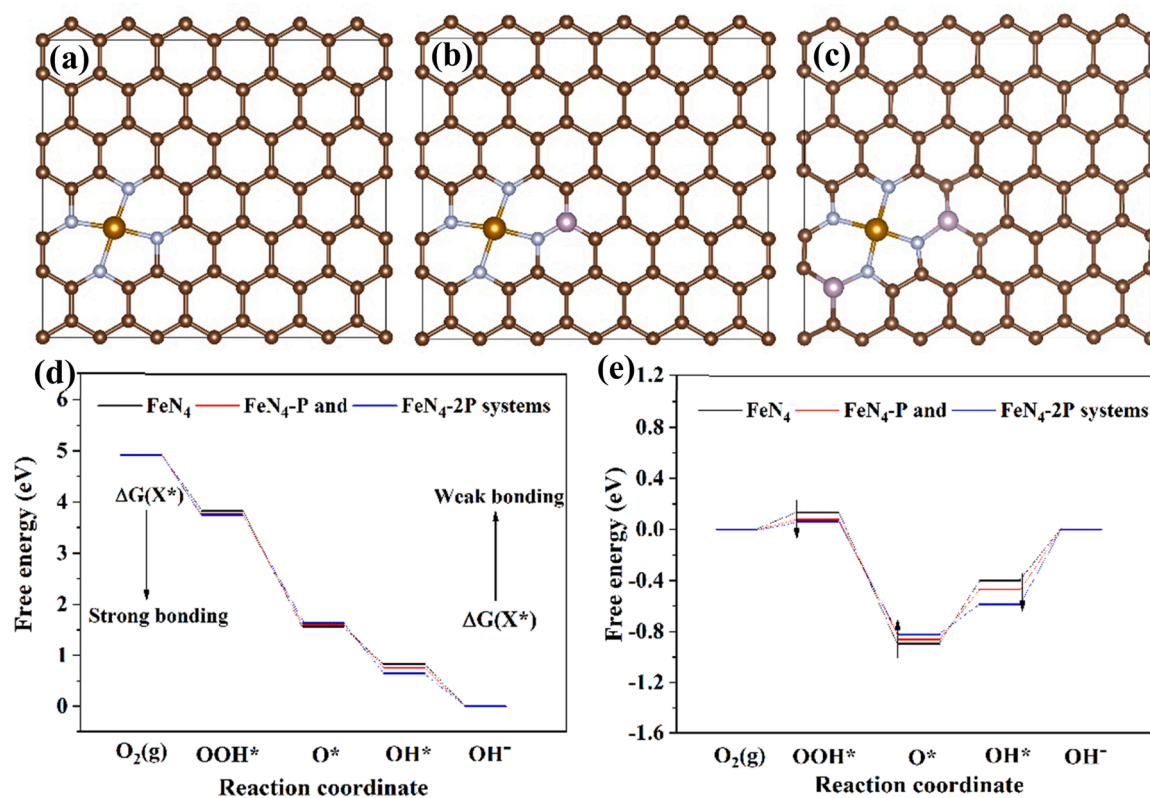
Fig. 5. Computational models for (a) Fe-N-C (FeN$_4$), (b) P-doped Fe-N-C (FeN$_4$-P), and (c) 2 P-doped Fe-N-C (FeN$_4$-2 P) systems. Free energy diagram of the Fe-N-C and P-doped Fe-N-C systems at (d) 0.00 V and (e) 1.23 V.
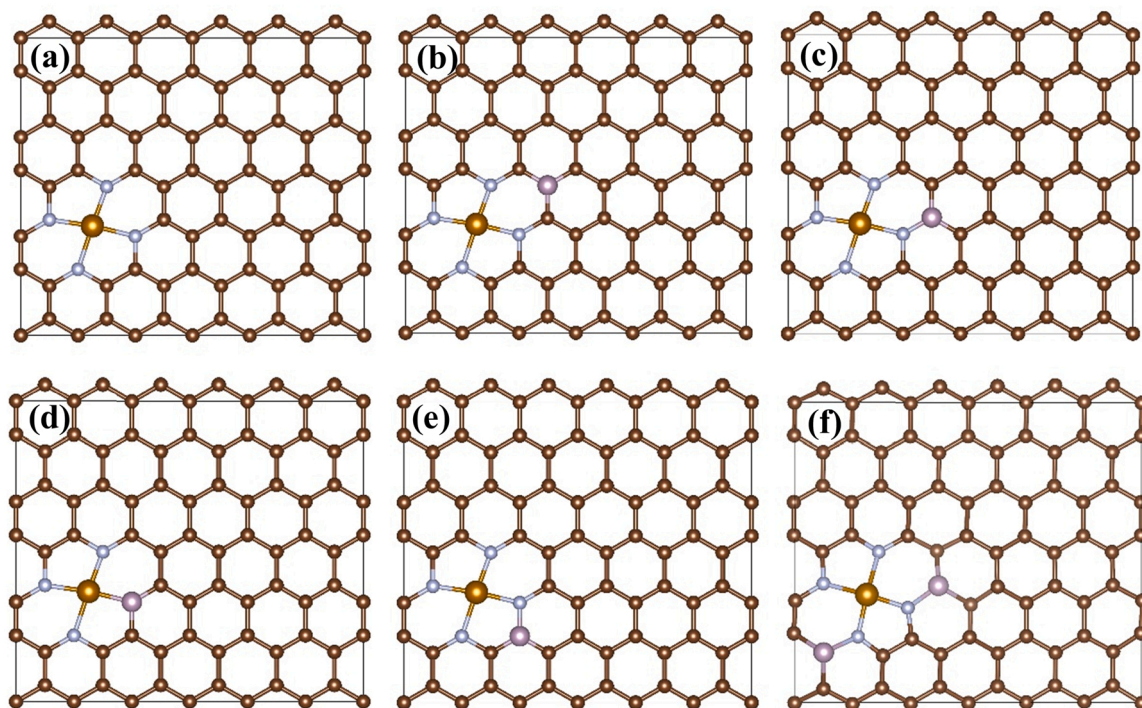

Fig. 6. Theoretical models for (a) FeN$_4$ and (b) FeN$_4$-P1, (c) FeN$_4$-P2, (d)FeN$_3$-P3, (e)FeN$_4$-P4, and (f) FeN$_4$-2 P systems. The brown, blue, and golden spheres represent carbon, nitrogen, and iron atoms respectively.

P dopants is unfordable for the ORR performance, since it can not only decrease the thermodynamic stability of the catalyst obviously (−5.140 eV, Table S7) but also lead to a much stronger OH* adsorbate.

The later factor will make the desorption of OH intermediates much more energetically unfavorable and is responsible for the obvious increased over potential. The calculation above confirms that a suitable
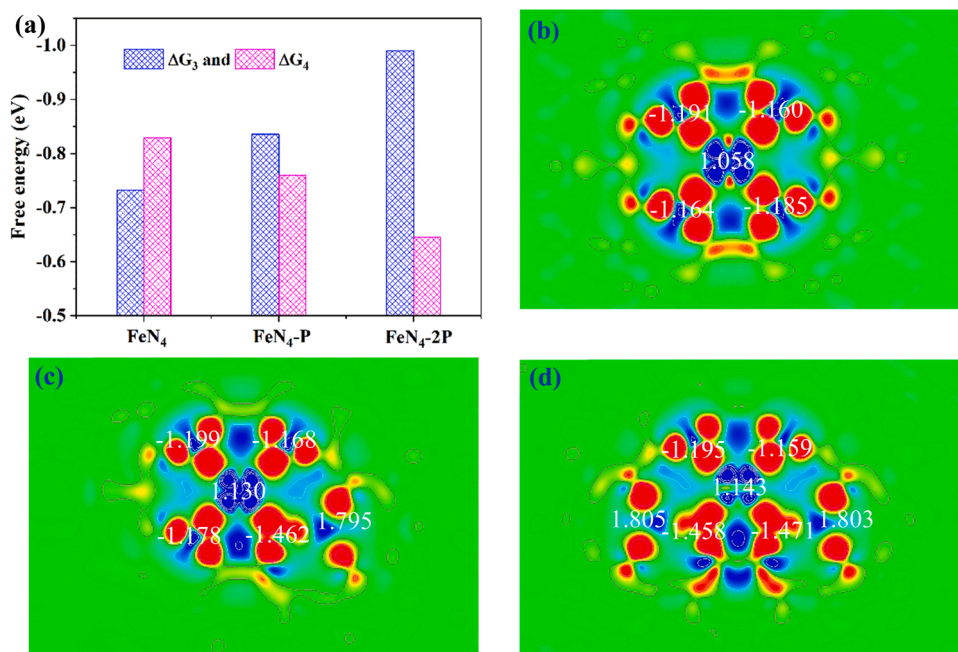
Fig. 7. (a) Free energy diagram of the third and fourth elementary steps for different catalysts and the planar electron density differences (EDDs) with Bader charges for (b) FeN$_4$, (c) FeN$_4$-P, and (d) FeN$_4$-2 P systems. The values of the color bar are ranged from − 0.02 (blue) to 0.02 (red).
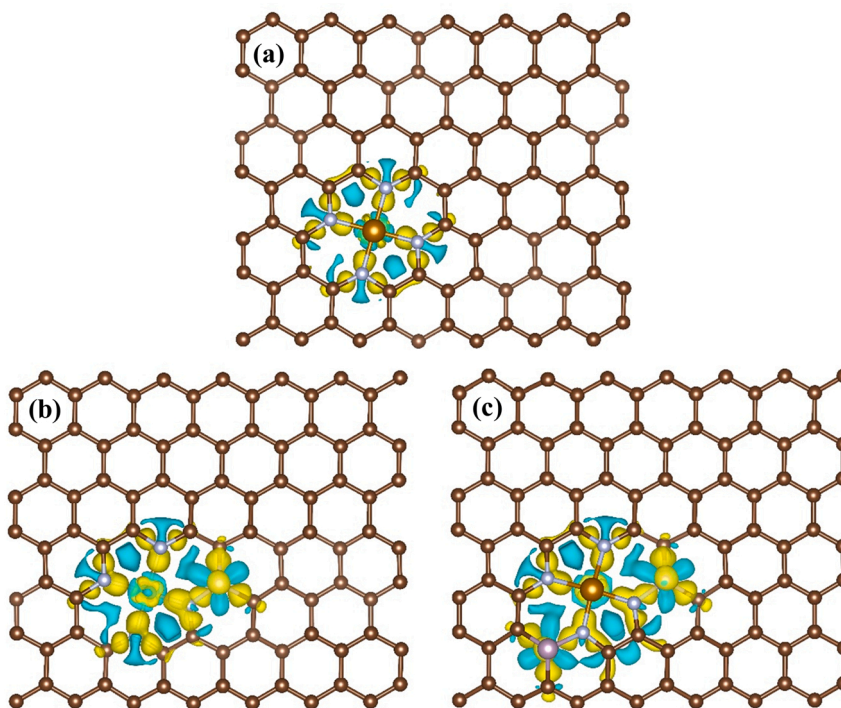
Fig. 8. Three-dimensional electron density differences (EDDs) for (a) FeN$_4$, (b) FeN$_4$-P and (c) FeN$_4$-2 P systems. The value for the iso-surface is 0.01.

amount of P dopants can modulate the local electronic structure near the active sites of the catalyst and result in an improved ORR performance, being consistent with the synergetic effect observed in the experiments.

4. Conclusion

In this work, we proposed a simple method for preparing expanded P-Fe-N-CNTs with high SSA by NaH$_2$PO$_2$ assisted process. The NaH$_2$PO$_2$ was used as P source and reducing agent, and a mixture of MIL-100 (Fe)

and ZIF-8 were used as precursor. The expanded P-Fe-N-CNTs exhibit excellent ORR properties with excellent E_{onset}, $E_{1/2}$ and long-term stability compared to Fe$_u$-N-CNTs nanotubes and commercial Pt/C electrodes. Benefit from excellent ORR performance, P-Fe-N-CNTs offers a high power density (145 mW cm^{-2}), large discharge specific capacity (885 mAh g^{-1}) and long-term stability (>144 h) in ZAB system. The outstanding ORR activity is mainly due to the synergistic effect of Fe-N$_x$/ P$_x$ and N-, P-co-doped carbon. More importantly, the Fe/N/P-tridoping and unique expanded structure of P-Fe-N-CNTs with large SSA can

promote charge transfer and mass transfer. The effect of the amount of P dopant on ORR activity is also discussed in DFT calculation. The results show that the adsorption strength of OOH* and OH* can be enhanced by proper P doping. Meanwhile, the appropriate P atom doping is beneficial to regulate the electronic structure around the catalytic site. The work offers a novel way for structural regulation of expanded nanotubes, which promotes effectively performance improvement of ORR and ZABs.

CRediT authorship contribution statement

Hui Chang: Writing, Data curation, Investigation, Conceptualization, **Ya-Fei Guo:** Data curation, Investigation, **Xu Liu:** Visualization, Review, **Peng-Fei Wang:** Review, **Ying Xie:** Data curation, Review, **Ting-Feng Yi:** Investigation, Supervision, Funding acquisition.

Declaration of Competing Interest

The authors declare that they have no known competing financial interests or personal relationships that could have appeared to influence the work reported in this paper.

Data Availability

No data was used for the research described in the article.

Appendix A. Supporting information

Supplementary data associated with this article can be found in the online version at doi:10.1016/j.apcatb.2023.122469.

References

[1] D. Chen, J. Zhu, X. Mu, R. Cheng, W. Li, S. Liu, Z. Pu, C. Lin, S. Mu, Nitrogen-Doped carbon coupled FeNi$_3$ intermetallic compound as advanced bifunctional electrocatalyst for OER, ORR and Zn-air batteries, Appl. Catal. B Environ. 268 (2020), 118729, https://doi.org/10.1016/j.apcatb.2020.118729.

[2] L. Zhong, C. Jiang, M. Zheng, X. Peng, T. Liu, S. Xi, X. Chi, Q. Zhang, L. Gu, S. Zhang, G. Shi, L. Zhang, K. Wu, Z. Chen, T. Li, M. Dahbi, J. Alami, K. Amine, J. Lu, Wood carbon based single-atom catalyst for rechargeable Zn–air batteries, ACS Energy Lett. 6 (2021) 3624–3633, https://doi.org/10.1021/acsenergylett.1c01678.

[3] X. Lu, L. Ge, P. Yang, O. Levin, V. Kondratiev, Z. Qu, L. Liu, J. Zhang, M. An, N-doped carbon nanosheets with ultra-high specific surface area for boosting oxygen reduction reaction in Zn-air batteries, Appl. Surf. Sci. 562 (2021) 150114, https://doi.org/10.1016/j.apsusc.2021.150114.

[4] X. Xu, X. Zhang, Z. Xia, R. Sun, H. Li, J. Wang, S. Yu, S. Wang, G. Sun, Solid phase microwave-assisted fabrication of Fe-doped ZIF-8 for single-atom Fe-N-C electrocatalysts on oxygen reduction, J. Energy Chem. 54 (2021) 579–586, https://doi.org/10.1016/j.jechem.2020.06.046.

[5] X. Lu, H. Xu, P. Yang, L. Xiao, Y. Li, J. Ma, R. Li, L. Liu, A. Liu, V. Kondratiev, O. Levin, J. Zhang, M. An, Zinc-assisted MgO template synthesis of porous carbon-supported Fe-Nx sites for efficient oxygen reduction reaction catalysis in Zn-air batteries, Appl. Catal. B Environ. 313 (2022) 121454, https://doi.org/10.1016/j.apcatb.2022.121454.

[6] Z. Chen, X. Zhong, Y. Xie, J. Liu, Z. Xu, R. Wang, A high-performance nitrogen-rich ZIF-8-derived Fe-NC electrocatalyst for the oxygen reduction reaction, J. Alloy. Compd. 884 (2021) 160980, https://doi.org/10.1016/j.jallcom.2021.160980.

[7] Y. Li, P. Zhang, L. Wan, Y. Zheng, X. Qu, H. Zhang, Y. Wang, K. Zaghib, J. Yuan, S. Sun, Y. Wang, Z. Zhou, S. Sun, A general carboxylate-assisted approach to boost the ORR performance of ZIF-derived Fe/N/C catalysts for proton exchange membrane fuel cells, Adv. Funct. Mater. 31 (2021), 2009645, https://doi.org/10.1002/adfm.202009645.

[8] H. Yang, Z. Li, S. Kou, G. Lu, Z. Liu, A complex-sequestered strategy to fabricate Fe single-atom catalyst for efficient oxygen reduction in a broad pH-range, Appl. Catal. B Environ. 278 (2020), 119270, https://doi.org/10.1016/j.apcatb.2020.119270.

[9] T. Zhang, S. Mao, P. Sun, X. Gao, H. Fang, H. Luo, W. Zhang, B. Zhou, Nanosized FeS/ZnS heterojunctions derived using zeolitic imidazolate Framework-8 (ZIF-8) for pH-universal oxygen reduction and High-efficiency Zn-air battery, J. Colloid Interf. Sci. 608 (2021) 446–458, https://doi.org/10.1016/j.jcis.2021.09.134.

[10] L. Zong, X. Chen, S. Dou, K. Fan, Z. Wang, W. Zhang, Y. Du, J. Xu, X. Jia, Q. Zhang, X. Li, Y. Deng, Y. Chen, L. Wang, Stable confinement of Fe/Fe$_3$C in Fe, N-codoped carbon nanotube towards robust zinc-air batteries, Chin. Chem. Lett. 32 (2021) 1121–1126, https://doi.org/10.1016/j.cclet.2020.08.029.

[11] L. Chai, Z. Hu, X. Wang, L. Zhang, T.-T. Li, J. Hu, J. Pan, J. Qian, S. Huang, Fe$_7$C$_3$ nanoparticles with in situ grown CNT on nitrogen doped hollow carbon cube with greatly enhanced conductivity and ORR performance for alkaline fuel cell, Carbon 174 (2021) 531–539, https://doi.org/10.1016/j.carbon.2020.12.070.

[12] Y. Zhang, R. Jiang, Z. Wang, Y. Xue, J. Sun, Y. Guo, Fe,N-codoped carbon nanotube)/(Fe-based nanoparticle) nanohybrid derived from Fe-doped g-C$_3$N$_4$: A superior catalyst for oxygen reduction reaction, J. Colloid Interface Sci. 579 (2020) 391–400, https://doi.org/10.1016/j.jcis.2020.06.057.

[13] H. Wang, F.X. Yin, N. Liu, R.H. Kou, X.B. He, C.J. Sun, B.H. Chen, D.J. Liu, H. Q. Yin, Engineering Fe–Fe$_3$C@Fe–N–C active sites and hybrid structures from dual metal–organic frameworks for oxygen reduction reaction in H$_2$–O$_2$ fuel cell and Li–O$_2$ battery, Adv. Funct. Mater. 29 (2019), 1901531, https://doi.org/10.1002/adfm.201901531.

[14] C. Feng, Y. Guo, S. Qiao, Y. Xie, L. Zhang, L. Zhang, W. Wang, J. Wang, 2-Methylimidazole as a nitrogen source assisted synthesis of a nano-rod-shaped Fe/FeN@N-C catalyst with plentiful FeN active sites and enhanced ORR activity, Appl. Surf. Sci. 533 (2020), 147481, https://doi.org/10.1016/j.apsusc.2020.147481.

[15] Y. Guo, A. Dong, Q. Huang, Q. Li, Y. Hu, J. Qian, S. Huang, Hierarchical N-doped CNTs grafted onto MOF-derived porous carbon nanomaterials for efficient oxygen reduction, J. Colloid Interf. Sci. 606 (2021) 1833–1841, https://doi.org/10.1016/j.jcis.2021.08.180.

[16] X. Xu, Z. Xia, X. Zhang, R. Sun, X. Sun, H. Li, C. Wu, J. Wang, S. Wang, G. Sun, Atomically dispersed Fe-N-C derived from dual metal-organic frameworks as efficient oxygen reduction electrocatalysts in direct methanol fuel cells, Appl. Catal. B Environ. 259 (2019), 118042, https://doi.org/10.1016/j.apcatb.2019.118042.

[17] Y. Meng, J.-C. Li, S.-Y. Zhao, C. Shi, X.-Q. Li, L. Zhang, P.-X. Hou, C. Liu, H.-M. Cheng, Fluorination-assisted preparation of self-supporting single-atom Fe-N-doped single-wall carbon nanotube film as bifunctional oxygen electrode for rechargeable Zn-Air batteries, Appl. Catal. B Environ. 294 (2021) 120239, https://doi.org/10.1016/j.apcatb.2021.120239.

[18] S.-H. Chae, A. Muthurasu, T. Kim, J.S. Kim, M.-S. Khil, M. Lee, H. Kim, J.Y. Lee, H. Y. Kim, Templated fabrication of perfectly aligned metal-organic framework-supported iron-doped copper-cobalt selenide nanostructure on hollow carbon nanofibers for an efficient trifunctional electrode material, Appl. Catal. B Environ. 293 (2021) 120209, https://doi.org/10.1016/j.apcatb.2021.120209.

[19] S.S.A. Shah, T. Najam, M.K. Aslam, M. Ashfaq, M.M. Rahman, K. Wang, P. Tsiakaras, S. Song, Y. Wang, Recent advances on oxygen reduction electrocatalysis: correlating the characteristic properties of metal organic frameworks and the derived nanomaterials, Appl. Catal. B: Environ. 268 (2020), 118570, https://doi.org/10.1016/j.apcatb.2019.118570.

[20] Y. Wang, J. Wang, D. Wei, M. Li, A. MOF-Protective-Pyrolysis, Strategy for the preparation of Fe-N-C catalysts and the role of Fe, N, and C in the oxygen reduction reaction in acidic medium, ACS Appl. Mater. Interfaces 11 (2019) 35755–35763, https://doi.org/10.1021/acsami.9b12638.

[21] L. Chen, H.F. Wang, C. Li, Q. Xu, Bimetallic metal-organic frameworks and their derivatives, Chem. Sci. 11 (2020) 5369–5403, https://doi.org/10.1039/d0sc01432j.

[22] A. Radwan, H. Jin, B. Liu, Z. Chen, Q. Wu, X. Zhao, D. He, S. Mu, 3D-ZIF scaffold derived carbon encapsulated iron nitride as a synergistic catalyst for ORR and zinc-air battery cathodes, Carbon 171 (2021) 368–375, https://doi.org/10.1016/j.carbon.2020.09.024.

[23] Z. Li, X. Wang, J. Nie, G. Ma, Electrospun bamboo-like Fe$_3$C encapsulated Fe-Si-N co-doped nanofibers for efficient oxygen reduction, J. Colloid Interf. 5466 (2019) 231–239, https://doi.org/10.1016/j.jcis.2019.03.079.

[24] X. Chu, F. Meng, T. Deng, W. Zhang, Metal organic framework derived porous carbon materials excel as an excellent platform for high-performance packaged supercapacitors, Nanoscale 13 (2021) 5570–5593, https://doi.org/10.1039/d1nr00160d.

[25] T. Tan, P. Tao, X. Li, S. Imhanria, J. Deng, W. Wang, Nitrogen-modified metal-organic framework-based carbon: An effective non-precious electrocatalyst for oxygen reduction reaction, Catal. Commun. 146 (2020) 106135, https://doi.org/10.1016/j.catcom.2020.106135.

[26] C. Yang, S. Shang, Q. Gu, J. Shang, X.-y Li, Metal-organic framework-derived carbon nanotubes with multi-active Fe-N/Fe sites as a bifunctional electrocatalyst for zinc-air battery, J. Energy Chem. 66 (2022) 306–313, https://doi.org/10.1016/j.jechem.2021.08.019.

[27] Y. Yao, H. Yin, H. Zhang, F. Wei, H. Hu, Y. Tang, S. Wang, Fe, Cu-coordinated ZIF-derived bimetal encapsulated N-doped carbon nanotube for efficient remediation

of various aqueous pollutants, Chem. Eng. J. 426 (2021), 131801, https://doi.org/10.1016/j.cej.2021.131801.

[28] Y. Li, M. Cui, Z. Yin, S. Chen, T. Ma, Metal-organic framework based bifunctional oxygen electrocatalysts for rechargeable zinc-air batteries: current progress and prospects, Chem. Sci. 11 (2020) 11646–11671, https://doi.org/10.1039/d0sc04684a.

[29] G. Kresse, J. Hafner, Ab initio molecular-dynamics for liquid-metals, Phys. Rev. B 47 (1993) 558–561, https://doi.org/10.1103/PhysRevB.47.558.

[30] G. Kresse, J. Hafner, Ab initio molecular-dynamics simulation of the liquid-metal amorphous-semiconductor transition in germanium, 1994, Phys. Rev. B 49 (1994) 14251–14269, https://doi.org/10.1103/PhysRevB.49.14251.

[31] G. Kresse, J. Furthmuller, Efficient iterative schemes for ab initio total-energy calculations using a plane-wave basis set, Phys. Rev. B 54 (1996) 11169–11186, https://doi.org/10.1103/PhysRevB.54.11169.

[32] G. Kresse, J. Furthmuller, Efficiency of ab-initio total energy calculations for metals and semiconductors using a plane-wave basis set, Comp. Mat. Sci. 6 (1996) 15–50, https://doi.org/10.1016/0927-0256(96)00008-0.

[33] P.E. Blöchl, Projector augmented-wave method, Phys. Rev. B 50 (1994) 17953–17979, https://doi.org/10.1103/PhysRevB.50.17953.

[34] J.P. Perdew, K. Burke, Ernzerhof M, Generalized gradient approximation made simple, Phys. Rev. Lett. 77 (1996) 3865–3868, https://doi.org/10.1103/PhysRevLett.77.3865.

[35] H.J. Monkhorst, J.D. Pack, Special points for Brillouin-zone integrations, Phys. Rev. B 13 (1976) 5188–5192, https://doi.org/10.1103/PhysRevB.13.5188.

[36] I.C. Man, H.Y. Su, C.-V. Federico, H.A. Hansen, J.I. Martínez, N.G. Inoglu, J. Kitchin, T.F. Jaramillo, J.K. Nørskov, J. Rossmeisl, Universality in oxygen evolution electrocatalysis on oxide surfaces, ChemCatChem 3 (2011) 1159–1165, https://doi.org/10.1002/cctc.201000397.

[37] S. Liu, Z. Li, C. Wang, W. Tao, M. Huang, M. Zuo, Y. Yang, K. Yang, L. Zhang, S. Chen, P. Xu, Q. Chen, Turning main-group element magnesium into a highly active electrocatalyst for oxygen reduction reaction, Nat. Commun. 11 (2020) 938, https://doi.org/10.1038/s41467-020-14565-w.

[38] P. Li, H. Wang, W. Fan, M. Huang, J. Shi, Z. Shi, S. Liu, Salt assisted fabrication of lignin-derived Fe, N, P, S codoped porous carbon as trifunctional catalyst for Zn-air batteries and water-splitting devices, Chem. Eng. J. 421 (2021), 129704, https://doi.org/10.1016/j.cej.2021.129704.

[39] C. Feng, S. Qiao, Y. Xie, L. Zhang, L. Zhang, W. Wang, J. Wang, 2-Methylimidazole as a nitrogen source assisted synthesis of a nano-rodshaped Fe/FeN@N-C catalyst with plentiful FeN active sites and enhanced ORR activity, Appl. Surf. Sci. 233 (2020), 147481, https://doi.org/10.1016/j.apsusc.2020.147481.

[40] H. Peng, K. Sun, X. Xie, H. Lei, G. Ma, Nitrogen-doped carbon nanoflowers with in situ generated Fe_3C embeded carbon nanotubes for efficient oxygen reduction electrocatalysts, Appl. Surf. Sci. 529 (2020), 147174, https://doi.org/10.1016/j.apsusc.2020.147174.

[41] P. Yu, L. Wang, Y. Xie, C. Tian, F. Sun, J. Ma, M. Tong, W. Zhou, J. Li, H. Fu, High-efficient, stable electrocatalytic hydrogen evolution in acid media by amorphous FexP coating Fe_2N supported on reduced graphene oxide, Small 14 (2018), e1801717, https://doi.org/10.1002/smll.201801717.

[42] X. Qu, Y. Han, Y. Chen, Y. Lin, G. Li, J. Yang, Y. Jiang, S. Sun, Stepwise pyrolysis treatment as an efficient strategy to enhance the stability performance of Fe-NX/C electrocatalyst towards oxygen reduction reaction and proton exchange membrane fuel cell, Appl. Catal. B: Environ. 295 (2021), 120311, https://doi.org/10.1016/j.apcatb.2021.120311.

[43] H. Pang, P. Sun, H. Gong, N. Zhang, J. Cao, R. Zhang, M. Luo, Y. Li, G. Sun, Y. Li, J. Deng, M. Gao, M. Wang, B. Kong, Wood-derived bimetallic and heteroatomic hierarchically porous carbon aerogel for rechargeable flow Zn-air batteries, ACS Appl. Mater. Interfaces 13 (2021) 39458–39469, https://doi.org/10.1021/acsami.1c10925.

[44] U.I. Kramm, I. Herrmann-Geppert, J. Behrends, K. Lips, S. Fiechter, P. Bogdanoff, On an easy way to prepare metal-nitrogen doped carbon with exclusive presence of MeN4-type sites active for the ORR, J. Am. Chem. Soc. 138 (2016) 635–640, https://doi.org/10.1021/jacs.5b11015.

[45] D. Xia, X. Yang, L. Xie, Y. Wei, W. Jiang, M. Dou, X. Li, J. Li, L. Gan, F. Kang, Direct growth of carbon nanotubes doped with single atomic Fe–N4 active sites and neighboring graphitic nitrogen for efficient and stable oxygen reduction electrocatalysis, Adv. Funct. Mater. 29 (2019), 1906174, https://doi.org/10.1002/adfm.201906174.

[46] Z. He, J.-L. Maurice, A. Gohier, C.S. Lee, D. Pribat, C.S. Cojocaru, Iron catalysts for the growth of carbon nanofibers: Fe, Fe_3C or Both, Chem. Mater. 23 (2011) 5379–5387, https://doi.org/10.1021/cm202315j.

[47] J.A. Rodriguez-Manzo, M. Terrones, H. Terrones, H.W. Kroto, L. Sun, F. Banhart, In situ nucleation of carbon nanotubes by the injection of carbon atoms into metal particles, Nat. Nanotechnol. 2 (2007) 307–311, https://doi.org/10.1038/nnano.2007.107.

[48] J.-M.B.C. Emmenegera, P. Mauron, P. Sudan, A. Lepora, B. Grobety, A. Zuttel, L. Schlapbach, Synthesis of carbon nanotubes over Fe catalyst on aluminium and suggested growth mechanism, Carbon 41 (2003) 539–547, https://doi.org/10.1016/s0008-6223(02)00362-7.

[49] H.K. Dipojono, A.G. Saputro, A.K. Fajrial, M.K. Agusta, F.T. Akbar, F. Rusydi, D.H.B. Wicaksono, Oxygen reduction reaction mechanism on a phosporus-doped pyrolyzed graphitic Fe/N/C catalyst, New J. Chem. 43 (2019) 11408–11418, https://doi.org/10.1039/c9nj02118c.

[50] R. Javed, M.A. Khan, D. Ye, Y. Zhao, L.A. Shah, J. Zhang, H. Zhao, Boosting oxygen reduction catalysis through electronic reconfiguration of Fe–N–C Induced by P doping, Electrocatalysis 12 (2021) 747–758, https://doi.org/10.1007/s12678-021-00682-7.